

## Forecast Evaluation of an Observing System Simulation Experiment Assimilating Both Radar and Satellite Data

THOMAS A. JONES

*Cooperative Institute for Mesoscale Meteorological Studies, University of Oklahoma, Norman, Oklahoma*

JASON A. OTKIN

*Cooperative Institute for Meteorological Satellite Studies, University of Wisconsin–Madison, Madison, Wisconsin*

DAVID J. STENSRUD

*Cooperative Institute for Mesoscale Meteorological Studies, University of Oklahoma,  
and NOAA/OAR/National Severe Storms Laboratory, Norman, Oklahoma*

KENT KNOPFMEIER

*Cooperative Institute for Mesoscale Meteorological Studies, University of Oklahoma, Norman, Oklahoma*

(Manuscript received 7 May 2013, in final form 22 July 2013)

### ABSTRACT

In the first part of this study, Jones et al. compared the relative skill of assimilating simulated radar reflectivity and radial velocity observations and satellite 6.95- $\mu\text{m}$  brightness temperatures  $T_B$  and found that both improved analyses of water vapor and cloud hydrometeor variables for a cool-season, high-impact weather event across the central United States. In this study, the authors examine the impact of the observations on 1–3-h forecasts and provide additional analysis of the relationship between simulated satellite and radar data observations to various water vapor and cloud hydrometeor variables. Correlation statistics showed that the radar and satellite observations are sensitive to different variables. Assimilating 6.95- $\mu\text{m}$   $T_B$  primarily improved the atmospheric water vapor and frozen cloud hydrometeor variables such as ice and snow. Radar reflectivity proved more effective in both the lower and midtroposphere with the best results observed for rainwater, graupel, and snow. The impacts of assimilating both datasets decrease rapidly as a function of forecast time. By 1 h, the effects of satellite data become small on forecast cloud hydrometeor values, though it remains useful for atmospheric water vapor. The impacts of radar data last somewhat longer, sometimes up to 3 h, but also display a large decrease in effectiveness by 1 h. Generally, assimilating both satellite and radar data simultaneously generates the best analysis and forecast for most cloud hydrometeor variables.

### 1. Introduction

Prior studies have shown that assimilating satellite and surface-based radar remote sensing observations using advanced data assimilation methods improves the analysis and forecast accuracy of numerical weather prediction (NWP) models with mesoscale (e.g., Vukicevic et al. 2004; Otkin 2010, 2012a,b; Jones et al. 2013a) and

convective scale (e.g., Vukicevic et al. 2006; Dowell et al. 2010, 2011; Polkinghorne and Vukicevic 2011; Jones et al. 2013b) resolutions. Satellite and radar data continuously sample the atmosphere at high spatial and temporal resolutions, beyond that possible from conventional observations such as radiosondes and surface stations. Assimilating radar and satellite observations separately has led to an increase in model skill for a variety of scales and atmospheric conditions; however, few studies have investigated the impact of their simultaneous assimilation.

Satellite sensors such as the Geostationary Operational Environmental Satellite (GOES) Imager and its

---

*Corresponding author address:* Dr. Thomas A. Jones, Cooperative Institute for Mesoscale Meteorological Studies, University of Oklahoma, and NOAA/OAR/National Severe Storms Laboratory, 120 David L. Boren Blvd., Norman, OK 73072.  
E-mail: thomas.jones@noaa.gov

successor, the Advanced Baseline Imager (ABI) to be included on GOES-R, sample top-of-the-atmosphere radiances in the visible, shortwave, and longwave infrared spectrums (Schmit et al. 2005). Assimilating radiances directly into NWP models using a radiative transfer model (RTM) is now common practice in operational global and continental-scale models with radiances accounting for the largest portion of the data volume (Moreau et al. 2004; Weng et al. 2007; English and Une 2006). Retrievals of temperature and humidity profiles from multispectral sounding instruments are also considered an important source of satellite data in NWP models (Li and Liu 2009; Liu and Li 2010). Assimilating either form of satellite data improves the characterization of the atmosphere in the model, especially in otherwise data-sparse regions such as over the oceans (e.g., Andersson et al. 1991; Mo et al. 1995; Derber and Wu 1998; Bouttier and Kelly 2001; Chevallier et al. 2004; McNally et al. 2006; Le Marshall et al. 2006; Xu et al. 2008; McCarty et al. 2009; McNally 2009; Collard and McNally 2009). Several assimilation techniques have been employed and include 3D and 4D variational methods (Rodgers 2000; McNally et al. 2000; Bouttier and Kelly 2001; Chevallier et al. 2004; McNally et al. 2006; Le Marshall et al. 2006; McCarty et al. 2009; McNally 2009; Collard and McNally 2009) as well as ensemble Kalman filter approaches (Vukicevic et al. 2006; Reale et al. 2008; Otkin 2010, 2012a,b; Stengel et al. 2010; Seaman et al. 2010; Jones et al. 2013a). The latter have proven particularly effective at assimilating satellite data since they are able to provide a flow-dependent and dynamically evolving estimate of the background error covariance (Kalman 1960; Evensen 1994; Heemink et al. 2001; Aksoy et al. 2009, 2010).

Surface based radars, such as the Weather Surveillance Radar-1988 Doppler (WSR-88D), provide valuable information about storm-scale winds and cloud and precipitation properties as inferred from 3D volume scans of radar reflectivity and radial velocity (Crum and Alberty 1993). Various cloud microphysical properties, such as phase, particle size, and number concentration can be inferred from the reflectivity data while their motion relative to the radar is sampled using radial velocity. During the past decade, many studies have examined the potential for assimilating radar data into storm-scale NWP models to improve the representation of convective precipitation within the model analysis (e.g., Weygandt et al. 2002; Snyder and Zhang 2003; Zhang et al. 2004; Xiao et al. 2005; Stensrud et al. 2009; Aksoy et al. 2009, 2010; Dowell et al. 2010, 2011). Many of these studies employ high-resolution (<5 km) grids that explicitly resolve the precipitation features

using variational techniques (e.g., Gao et al. 1999, 2004; Weygandt et al. 2002; Xiao et al. 2005; Gao and Stensrud 2012). Additional studies have focused on using an ensemble approach (Snyder and Zhang 2003; Zhang et al. 2004; Aksoy et al. 2010; Yussouf and Stensrud 2010; Dowell et al. 2011). Results have shown that assimilating radar data using either technique improves the characterization of convection and the near-storm environment within these high-resolution models.

Jones et al. (2013a) assimilated satellite brightness temperatures  $T_B$  and radar reflectivity and radial velocity data using an observing system simulation experiment (OSSE) for a cold-season case study occurring on 24 December 2009. The results indicated that assimilating satellite brightness temperatures  $T_B$  reduced errors for mid- and upper-tropospheric water vapor mixing ratio as well as frozen cloud hydrometeor variables. Impacts were smaller in the lower troposphere because of reduced sensitivity for the satellite observations. Radar data generally had a larger positive impact than the satellite data, primarily due to the much higher-resolution vertical profile information. As a result, improvements to humidity and cloud hydrometeor variables were observed at all atmospheric levels with Doppler radial velocity information also resulting in a significant reduction in wind velocity errors. Assimilating both satellite and radar data generally produced the most accurate cloud and thermodynamic analyses, indicating that both are providing unique information to the model.

Jones et al. (2013a) primarily focused on the analysis accuracy obtained after 1 h of assimilating satellite and radar observations. In this study, their results are extended to include additional analysis to determine the potential impact of assimilating each dataset on specific cloud-related state variables. Results presented herein are computed using the experiments described in Jones et al. (2013a), starting at the final analysis time of 1200 UTC 24 December and continuing over a 3-h forecast period to 1500 UTC. The introduction is followed by a discussion of the truth simulation and corresponding simulated observations in section 2. Section 3 discusses the overall experiment design while section 4 provides an analysis of correlations between simulated remote sensing products with water vapor and cloud hydrometeor variables. Section 5 summarizes the results found by Jones et al. (2013a). Section 6 discusses the comparison of moisture and cloud hydrometeor forecasts between truth and each experiment as a function of time. Section 7 shows a similar comparison using simulated satellite  $T_B$  and radar reflectivity. Section 8 summarizes the results and provides the conclusions.

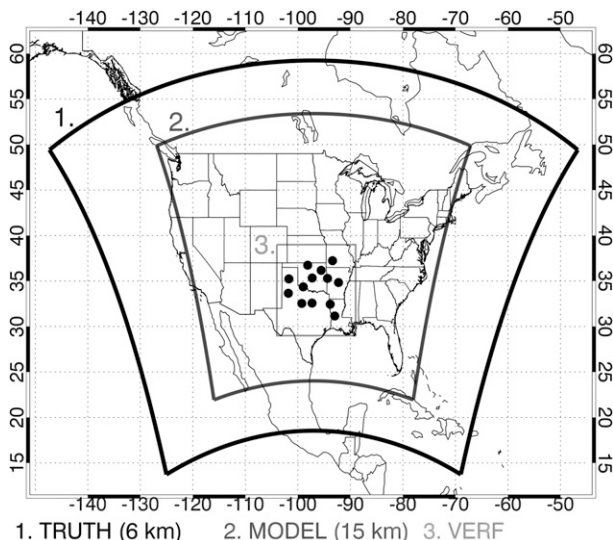


FIG. 1. Domains used in this study: domain 1, truth simulation; domain 2, forecast model; and domain 3, verification. All domains have a horizontal resolution of 15 km with 52 vertical levels. The 13 WSR-88Ds simulated are located within the verification domain.

## 2. Truth simulation and simulated observations

### a. Simulation characteristics

A truth simulation depicting the evolution of a strong midlatitude cyclone and associated precipitation across the central United States on 24 December 2009 was generated using the Advanced Research Weather Research and Forecasting Model (ARW-WRF), version 3.3 (Skamarock et al. 2008), hereafter labeled as “truth.” Global 0.5° Final Analyses (FNL) provide initial and boundary conditions for the simulation starting at 0000 UTC 23 December 2009 on a continental U.S. (CONUS) domain with 6-km horizontal grid spacing ( $1100 \times 750$ ) and 52 vertical levels (Fig. 1), which is integrated over the next 48 h and output at 5-min intervals. The truth simulation uses the WRF single moment 6-class microphysics scheme (Hong and Lim 2006), the Yonsei University planetary boundary layer scheme (Hong et al. 2006), the Kain–Fritsch cumulus parameterization scheme (Kain and Fritsch 1993; Kain 2004), and the Rapid Radiative Transfer Model (RRTM) longwave and shortwave radiation schemes (Iacono et al. 2008) to parameterize subgrid-scale processes. The Noah land surface model is used to compute surface heat and moisture fluxes.

### b. Simulated observations

Simulated observations are generated from truth for observation types representing conventional, satellite, and radar data. Conventional observations include those

from Automated Surface Observing System (ASOS), Aircraft Communications Addressing and Reporting System (ACARS), and radiosonde instruments. Observation types include temperature, humidity, wind speed and direction, and surface pressure observations. Observation errors are drawn from uncorrelated Gaussian error distributions that are based on a given sensor’s accuracy.

Simulated infrared 6.95- $\mu\text{m}$   $T_B$  are computed using the Successive Order of Interaction (SOI) forward radiative transfer model developed by Heidinger et al. (2006). This band is sensitive to water vapor content in the mid- and upper troposphere. The simulated ABI observations are computed every 5 min on the 6-km truth grid, which are then averaged to a 30-km resolution prior to assimilation. Synthetic WSR-88D reflectivity and radial velocity observations are generated from the truth simulation for 13 radar locations in the south-central United States (Fig. 1) at 5-min intervals from 1100 to 1200 UTC 24 December 2009 using the radar simulator contained within the Data Assimilation Research Testbed (DART) software (Anderson et al. 2009). Observations are obtained using the volume coverage pattern (VCP) 21 WSR-88D scan strategy with a 6° in azimuthal increment (Crum and Alberty 1993). Simulated radar gate length is set at 15 km, with the closest and farthest gates at 3 and 240 km, respectively. Further details of the truth simulation and corresponding observations are available in Jones et al. (2013a).

## 3. Experiment design

The experiment design closely follows that previously laid out by Otkin et al. (2011) and Jones et al. (2013a). In summary, a 48-member WRF ensemble with perturbed initial and lateral boundary conditions is generated from Global Forecast System (GFS) analysis fields at 6-h intervals starting at 0000 UTC 23 December 2009. The assimilation experiments employed the same vertical resolution (52 levels) and physics options as the truth simulation, but were performed over a smaller spatial domain containing 15-km horizontal grid spacing ( $272 \times 216$  grid points) (Fig. 1). The ensemble freely evolves starting at 0000 UTC 23 December and continues until 0900 UTC 24 December. Beginning at 0900 UTC, simulated conventional temperature, wind, and surface pressure observations are assimilated at 5-min intervals until 1100 UTC 24 December.

At 1100 UTC, four assimilation experiments are initiated, with observations assimilated every 5 min until 1200 UTC. The first experiment represents the control case (CONV) in which only conventional observations are assimilated (Table 1). Other experiments are performed in which simulated ABI 6.95- $\mu\text{m}$   $T_B$  are assimilated

TABLE 1. Observation types assimilated into each experiment.

Expt	Observation types
CONV	Conventional observations only (ASOS, ACARS, raob)
SAT	Conventional + 6.95- $\mu\text{m}$ ABI clear and cloudy radiances
RAD	Conventional + radar reflectivity and radial velocity
RADSAT	Conventional + radar + satellite

across the entire CONUS domain and WSR-88D reflectivity and radial velocity were assimilated from 13 radar locations across the southern plains, in addition to conventional observations. These experiments are referred to as SAT and RAD, respectively. The final experiment (RADSAT) combines both satellite and radar data with conventional observations to assess their combined impact. Building on the Jones et al. (2013a) study that focused on the data assimilation period, in this study, the forecast impact is examined for each experiment. Short-range ensemble forecasts are performed using the final ensemble analyses for each experiment for a 3-h period starting at 1200 UTC. Figure 1 shows the assimilation and verification domains used for this study.

#### 4. Observation correlation analysis

As discussed in the introduction, Jones et al. (2013a) showed that assimilating ABI 6.95- $\mu\text{m}$   $T_B$  and WSR-88D

reflectivity and radial velocity observations produced more accurate model analyses at 1200 UTC, with the greatest impacts observed in the water vapor and cloud hydrometeor mixing ratios in the mid- and upper troposphere. To more closely examine these results, the sensitivity of satellite and radar observations to the water vapor and cloud fields as a function of height is explored in this section through a correlation analysis. Correlations are computed using the satellite and radar observations located within the verification domain (refer to Fig. 1) at 1200 UTC and the corresponding water vapor and cloud hydrometeor fields from the truth simulation. Data from the truth simulation are used for this analysis rather than the first guess from the assimilation experiments to eliminate the influence of localization and sampling errors on the correlations, as well as to remove smoothing artifacts introduced when calculating the ensemble mean. The correlations derived from the truth simulation should be representative of the impact of the remote sensing data on the various hydrometeor variables.

Figure 2a shows the correlation between the water vapor mixing ratio (QVAPOR) as a function of height and simulated ABI 6.95- $\mu\text{m}$   $T_B$  from the truth simulation. As expected, the variables are inversely related over most of the troposphere, with colder  $T_B$  corresponding to higher QVAPOR values because the peak of the weighting function profile occurs higher in the atmosphere with increasing water vapor content (refer to Fig. 3a in Jones et al. 2013a). Comparing clear- and

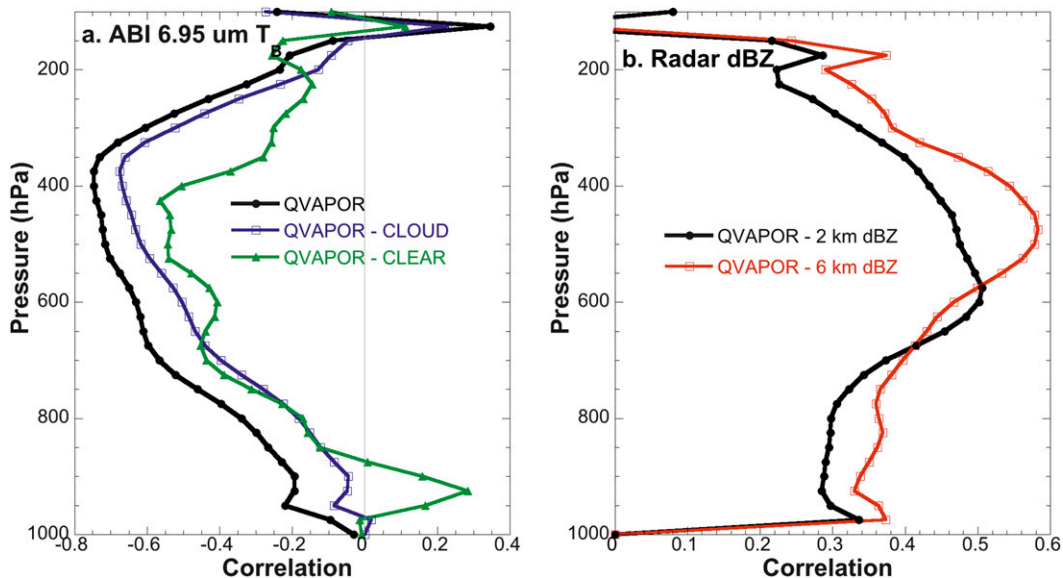


FIG. 2. (a) Correlation between simulated ABI 6.95- $\mu\text{m}$   $T_B$  and water vapor mixing ratio (QVAPOR) as a function of height for all, clear, and cloudy observations in the verification domain at 1200 UTC from the truth simulation. (b) Correlation between 2- and 6-km simulated radar reflectivity where reflectivity is  $>0$  dBZ.

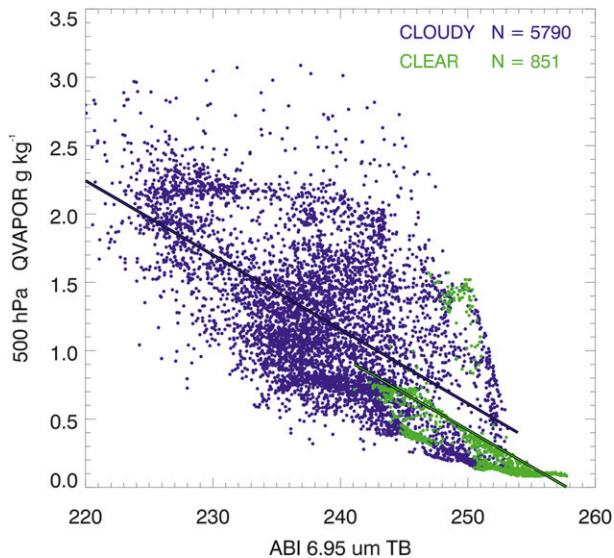


FIG. 3. Scatterplot of clear (green) and cloudy (purple) ABI 6.95- $\mu\text{m}$   $T_B$  and water vapor mixing ratio (QVAPOR) at 500 hPa at 1200 UTC from the truth simulation. Best-fit linear regression lines are overlaid for both clear and cloudy samples.

cloudy-sky samples reveals that both have similar correlation profiles though their magnitudes are somewhat less than the combined sample (Fig. 2a). Cloudy model grid points are defined as those where the total integrated column combined liquid and frozen cloud mixing ratios is  $>0.01 \text{ g kg}^{-1}$ . Overall, the correlation between clear-sky  $T_B$  and QVAPOR is lower than for cloudy-sky observations, which is somewhat surprising. One potential explanation is that the cloudy-sky sample size is over 6 times larger than the clear-sky sample (5790 vs 851); thus, outliers have a greater impact on the latter. A scatterplot of 500-hPa QVAPOR and 6.95- $\mu\text{m}$   $T_B$  indicates this to be the case with the clear sample generally confined to  $T_B > 240 \text{ K}$  and  $\text{QVAPOR} < 1.0 \text{ g kg}^{-1}$  (Fig. 3). However, several outliers are present in the clear sample where  $\text{QVAPOR} > 1.0 \text{ g kg}^{-1}$ , reducing the overall magnitude of the correlation, also evident by their distance from the best-fit linear regression line. The cloudy sample is somewhat noisy, but also has the much larger sample size. In cloudy-sky regions, there will also typically be a deeper saturated layer beneath the cloud top, thereby increasing correlations between 6.95- $\mu\text{m}$   $T_B$  and the water vapor field over a greater depth of the atmosphere.

Simulated radar reflectivity observations also show a strong correlation with QVAPOR, though the maximum values are generally less than for satellite data (Fig. 2b). The statistics are computed using radar reflectivity at 2-km and 6-km AGL to determine if there is sensitivity to the observation height. Only those observations with

a reflectivity  $>0 \text{ dBZ}$  are used. Overall, radar reflectivity and QVAPOR are positively correlated, indicating that higher reflectivity corresponds to higher QVAPOR values. Correlations are maximized near 600 hPa for the 2-km observations and near 500 hPa for the 6-km reflectivity observations. Higher correlations occur at most levels for the 6-km observations, indicating a closer relationship between radar reflectivity and water vapor, possibly because of less spatial variability at higher levels. Despite radar reflectivity not being directly sensitive to atmospheric water vapor aside from assumed saturation in the presence of clouds, modest correlations exist throughout the troposphere. Because radar reflectivity is sensitive to precipitating hydrometeors, the relatively high correlations are likely due to the presence of saturated cloud layers both above and below the precipitation, similar to that found for the satellite observations in Fig. 2a. As a result, high reflectivity corresponds to higher atmospheric water vapor content indicating that assimilating radar reflectivity can also improve the QVAPOR analysis. The most direct relationship remains with the 6.95- $\mu\text{m}$   $T_B$  generating higher correlations in the midtroposphere compared to radar reflectivity.

Figure 4a shows the correlation between simulated 6.95- $\mu\text{m}$   $T_B$  and radar reflectivity and various cloud hydrometeor variables present in the model analysis. The total cloud hydrometeor mixing ratio (QALL) is defined as the summation of cloud liquid water (QCLOUD), cloud ice (QICE), graupel (QGRAUP), snow (QSNOW), and rain (QRAIN) mixing ratios (Otkin 2010; Jones et al. 2013a). This variable was created to provide a measure of the effects of assimilating both satellite and radar data on the bulk characteristics of the cloud field. Inspection of Fig. 4a shows that substantial differences exist in the correlation profiles for the 6.95- $\mu\text{m}$   $T_B$  observations. The highest correlations exist for QICE and QSNOW, with the maximum values occurring in the mid- and upper troposphere. Correlations for QGRAUP and especially QCLOUD are generally lower. Interestingly, the correlation between QRAIN and 6.95- $\mu\text{m}$   $T_B$  is surprisingly large below 700 hPa, indicating a modest sensitivity to liquid raindrops (Fig. 3). It is unlikely that 6.95- $\mu\text{m}$   $T_B$  are sensitive to these drops directly, but instead suggests a closer relationship between higher ice and snow concentrations aloft, which are directly sensed from the satellite, and precipitating hydrometeors in the lower troposphere. These results indicate that assimilating 6.95- $\mu\text{m}$   $T_B$  should have its greatest impact on the snow and ice variables with a potential impact on rain, which is consistent with the findings of Jones et al. (2013a). Last, nearly constant correlations around  $\sim 0.5$  occur throughout the depth of

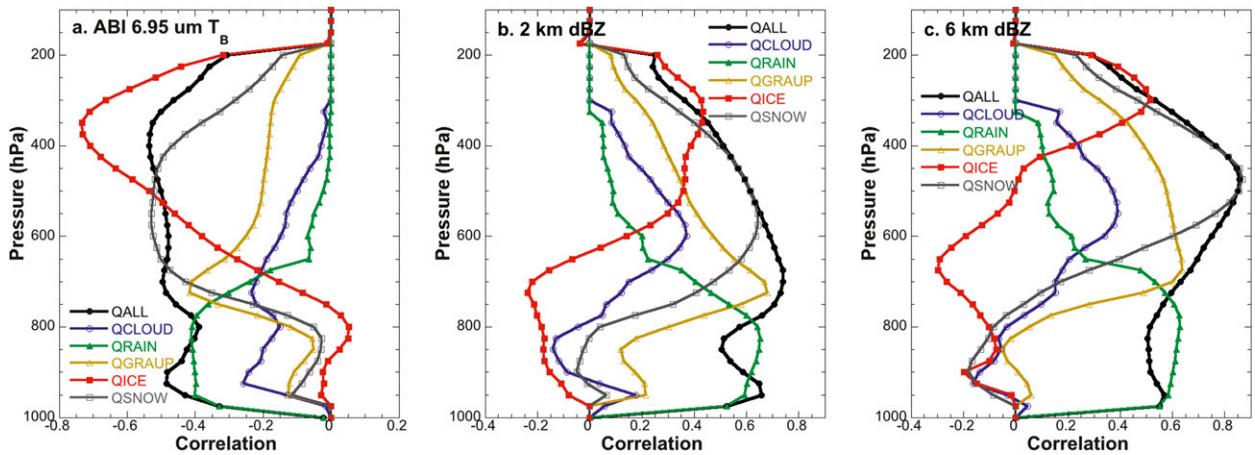


FIG. 4. As in Fig. 2, but for cloud hydrometeor variables (QALL, QCLOUD, QRAIN, QGRAUP, QICE, and QSNOW) correlated with (a) ABI 6.95- $\mu\text{m}$   $T_B$ , (b) 2-km radar reflectivity, and (c) 6-km radar reflectivity.

the troposphere for QALL, with lower  $T_B$  corresponding to higher cloud mixing ratios, similar to that present for QVAPOR.

Correlation profiles between the cloud species and 2- and 6-km radar reflectivity observations are shown in Figs. 4b,c. The correlations are generally positive indicating that higher reflectivity correspond to larger hydrometeor mixing ratio values. The correlation between 2-km reflectivity and QALL is  $>0.5$  from the surface to 400 hPa. Below 800 hPa, QRAIN accounts for much of this correlation. This is expected since radar reflectivity is more sensitive to rain than to the other hydrometeor species. Above 800 hPa, the correlations increase for QGRAUP and QSNOW due to the presence of more frozen hydrometeors aloft. As with 6.95- $\mu\text{m}$   $T_B$ , the correlation between reflectivity and QCLOUD is generally lowest. Correlation profiles for the 6-km reflectivity observations show similar characteristics (Fig. 4c), with the primary difference being that larger correlations occur and are maximized higher in the atmosphere. The higher QALL correlations in the upper troposphere are primarily due to the higher QSNOW correlation since at 6-km radar reflectivity is primarily sensing snow hydrometeors.

In summary, the relatively high correlations indicate that satellite and radar reflectivity observations should have a significant impact on water vapor and cloud hydrometeor variables when assimilated. In particular, the satellite data should be most effective with improving the QICE and QSNOW fields in the mid- and upper troposphere, while radar is likely to have greater impacts on QRAIN, QGRAUP, and QSNOW throughout the atmospheric column.

## 5. Comparison with 1200 UTC assimilation results

Jones et al. (2013a) provided a thorough analysis of the effects of assimilating simulated satellite and radar data between 1100 and 1200 UTC with an emphasis placed on the final analysis at 1200 UTC. The results of that work are summarized here for reference and in the context of the correlation statistics described above. All experiments show a moist bias between the surface and 700 hPa with a smaller dry bias above at 1200 UTC (Fig. 5a). SAT reduces the magnitude of the bias in this lower layer, but also increases RMSD slightly compared to CONV, which is consistent with the low correlation between QVAPOR and 6.95- $\mu\text{m}$   $T_B$  in the lower atmosphere observed in Fig. 2a. In the midtroposphere where the magnitude of the correlation is higher, SAT lowers RMSD compared to CONV. The RAD experiment also reduces RMSD compared to CONV from 900 up to at least 400 hPa above which moisture concentrations and correlations between QVAPOR and radar reflectivity are small (Figs. 2a and 5a). Most of the improvement in QVAPOR error can be attributed to assimilating radar reflectivity rather than radial velocity because it is more strongly correlated to atmospheric moisture content (not shown).

Strong correlations between QALL and both remote sensing observation types (Fig. 4) translate into reductions in RMSD at several model levels depending on whether satellite or radar data are being assimilated (Fig. 6). SAT produces the greatest reduction in RMSD in the 700–300-hPa layer generally corresponding to the levels of maximum correlation (Figs. 4a and 6a). RAD reduces RMSD compared to SAT (and CONV) at all levels consistent with its higher correlation values

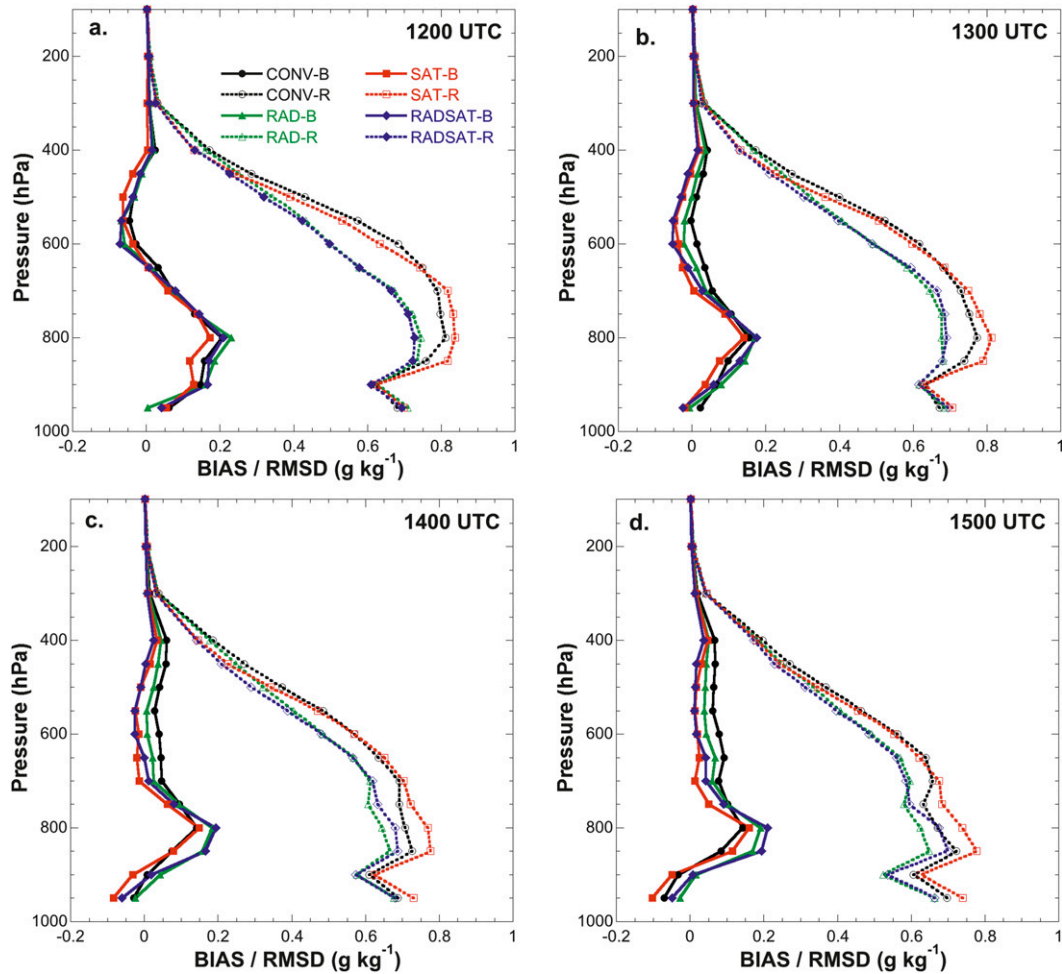


FIG. 5. Vertical profile of bias (“B”) and RMSD (“R”) for QVAPOR at (a) 1200, (b) 1300, (c) 1400, and (d) 1500 UTC representing the analysis time and 1-, 2-, and 3-h forecast, respectively.

(0.6 vs  $-0.4$ , Figs. 4a and 6a). QCLOUD from CONV and SAT have almost identical RMSD profiles indicating that the assimilation of  $6.95\text{-}\mu\text{m } T_B$  have little impact, which is consistent with the low correlation found between these two variables (Figs. 2b and 6b). Radar reflectivity is also weakly correlated to QCLOUD, but it does manage to reduce RMSD compared to CONV by  $0.03\text{ g kg}^{-1}$ . QRAIN has a high correlation with radar reflectivity (Figs. 4b,c); thus, RAD reduces RMSD compared to CONV below 600 hPa where liquid water drops are present (Fig. 6c). The modest correlation with satellite  $T_B$  is also apparent through a small but consistent reduction in RMSD for SAT compared to CONV (Figs. 2b and 6c). For QGRAUP, biases are near zero at most levels for all experiments with RMSD errors maximized at the 650-hPa level (Fig. 6d). A small decrease in RMSD occurs in SAT compared to CONV between 650 and 400 hPa. The correlation between satellite  $T_B$  and QGRAUP is maximized near 700 hPa, but

the maximum value is only  $-0.4$  (Fig. 4a). In the case of RAD, QGRAUP RMSD is reduced by nearly half compared to the CONV value in the midtroposphere (Fig. 6e). High correlations exist between radar reflectivity (especially at 6 km) and QGRAUP at these levels suggesting the positive impact observed in the error calculations.

For the QICE field, SAT should have its greatest impact near 400 hPa corresponding to correlation values of at least  $-0.7$  (Fig. 2a). The reduction in RMSD in SAT compared to CONV indeed is maximized at these levels (Fig. 6e). For RAD, the picture is somewhat more complex owing to the negative correlations between QICE and radar reflectivity in the lower half of the atmosphere (Figs. 4b,c). As a result, RAD only shows marginal skill compared to CONV at these levels, which improves with height as the correlations become positive. Finally, large differences are present in QSNOW with the maximum RMSD reduction occurring at 500 hPa for

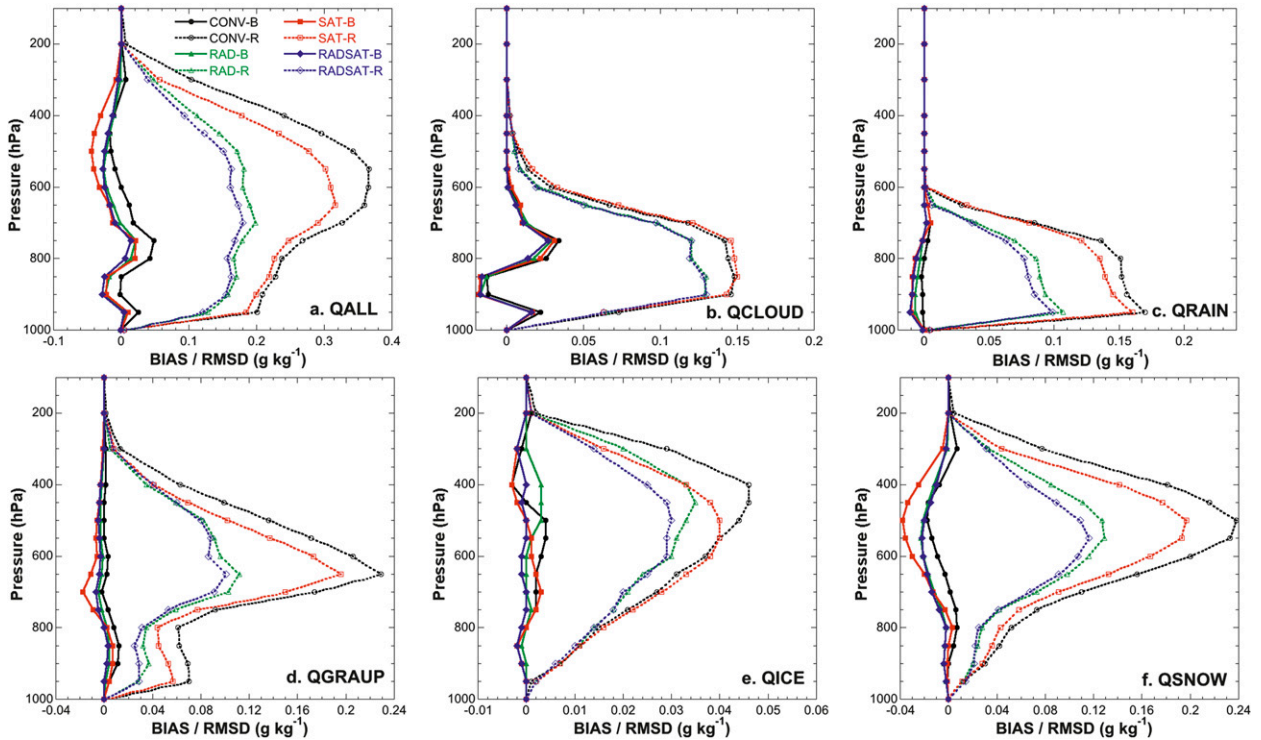


FIG. 6. Vertical profile of bias (“B”) and RMSD (“R”) for (a) QALL, (b) QCLOUD, (c) QRAIN, (d) QGRAUP, (e) QICE, and (f) QSNOW calculated over the verification domain for each experiment at 1200 UTC 24 Dec.

both SAT and RAD (Fig. 6f). This corresponds well to the levels of maximum correlation between QSNOW and satellite  $T_B$  or radar reflectivity. The higher correlation coefficient for radar reflectivity corresponds with a larger reduction in RMSD for RAD compared to SAT (Fig. 6f).

## 6. Forecast moisture and cloud errors

### a. Water vapor mixing ratio ( $QVAPOR$ )

Results from Jones et al. (2013a) indicate that assimilating ABI  $6.95\text{-}\mu\text{m}$   $T_B$  and WSR-88D reflectivity had positive impacts on moisture and cloud hydrometeor variables in the analysis. Here, we examine the forecast accuracy of these variables for a 3-h forecast period starting at 1200 UTC 24 December. Ensemble forecasts are performed for each experiment using the final ensemble analyses obtained at the end of the assimilation period.

Figure 7a shows time series of ensemble mean 500-hPa  $QVAPOR$  bias and RMSD for each experiment. Throughout the forecast period, CONV contains the highest RMSD with SAT providing a consistent  $0.02\text{ g kg}^{-1}$  improvement. Assimilating radar data initially reduces RMSD up to  $0.05\text{ g kg}^{-1}$  at 1200 UTC, but the impact

decreases to  $0.025\text{ g kg}^{-1}$  by 1500 UTC. The RADSAT experiment performs best at all times, indicating that the superior analysis accuracy achieved when both datasets are assimilated persists during the forecast period. All experiments show a small dry bias at 1200 UTC, which slowly changes to a wet bias later in the forecast period. Assimilating either satellite or radar data appears to dry the midtroposphere compared to CONV producing lower bias and RMSD at the end of the forecast cycle.

In the lower troposphere (Fig. 8a), RMSD are  $\sim 0.05\text{ g kg}^{-1}$  larger during the SAT case compared to CONV at all forecast times, which indicates that  $6.95\text{-}\mu\text{m}$   $T_B$  assimilation has a negative forecast impact here (Fig. 8a). Conversely, RAD lowers RMSD a similar amount compared to CONV indicating that radar data continue to provide useful information near the surface. These results are consistent with the tendency for the satellite observations to be most sensitive to clouds and water vapor in the mid- and upper troposphere, whereas radar observations are sensitive to features throughout the troposphere due to their greater 3D coverage.

The vertical distributions of bias and RMSD for water vapor averaged over the verification domain are shown in Figs. 5b,c,d for the 1-, 2-, and 3-h forecast times, respectively. These figures show that the forecast impact

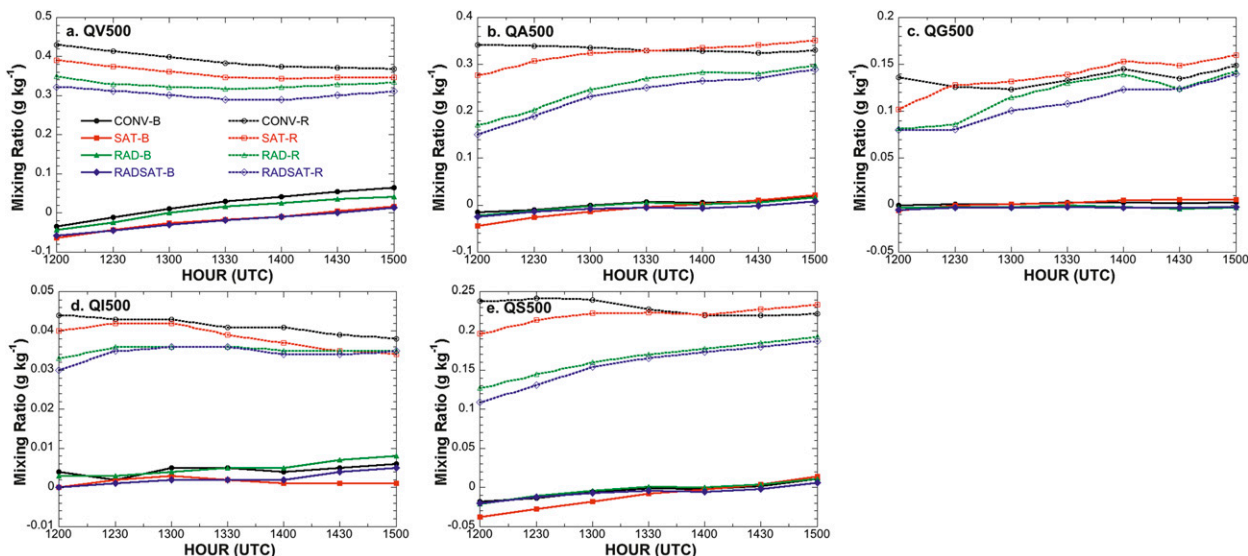


FIG. 7. Time series of bias (“B”) (experiment – truth) and RMSD (“R”) for (a) 500-hPa water vapor mixing ratio (QV500), (b) total cloud water mixing ratio (QA500), (c) graupel mixing ratio (QG500), (d) cloud ice mixing ratio (QI500), and (e) snow mixing ratio (QS500) between 1200 and 1500 UTC 24 Dec. Bias and RMSD statistics are calculated within the verification domain only.

of satellite and radar data assimilation varies greatly as a function of height and time. At 1300 UTC, the bias profiles for all experiments remain similar to those found at 1200 UTC with a small moist bias centered around 800 hPa and a smaller dry bias maximized near 600 hPa (Fig. 6b). The SAT experiment contains higher RMSD than CONV below 700 hPa with improvements confined to higher levels, consistent with the time series in Figs. 7 and 8. By 1500 UTC, the dry bias above 600 hPa

had disappeared; however, the low-level moist bias persists (Fig. 6d). At this time, the vertical profile of RMSD below 700 hPa loses its smooth nature with larger errors values than the 1-h forecast. One result that is clear is that the effects of assimilating both datasets are apparent out to at least a 3-h forecast. However, the negative impact of satellite data assimilation below 700 hPa indicates a need for better low-level moisture information from satellite observations.

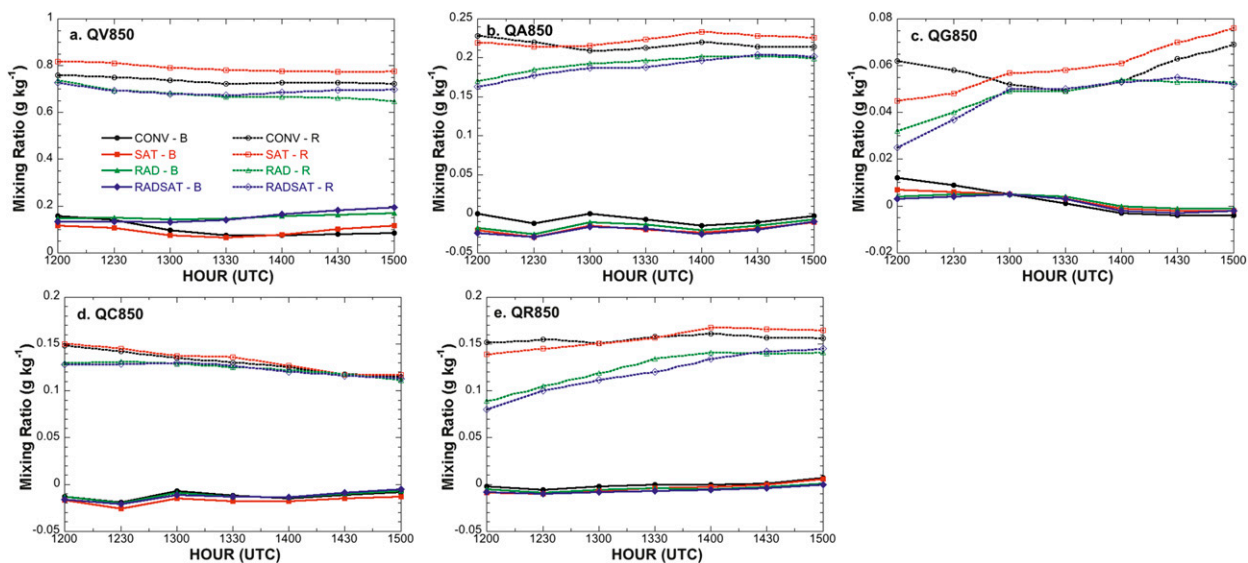


FIG. 8. As in Fig. 7, but calculated for 850-hPa data. Ice and snow mixing ratios at this level are small and replaced with (d) cloud liquid water mixing ratio (QC850) and (e) rain mixing ratio (QR850).

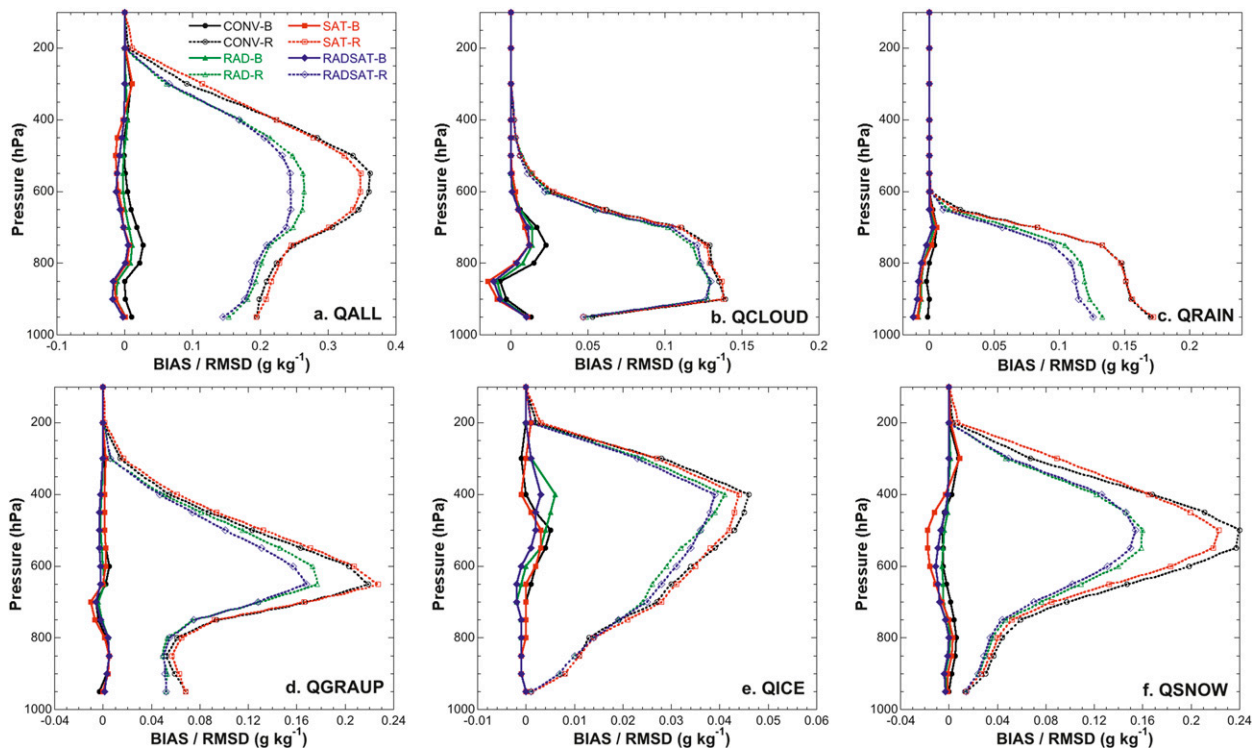


FIG. 9. As in Fig. 6, but for 1-h forecasts at 1300 UTC.

### b. Total cloud water mixing ratio (*QALL*)

Figure 7b shows the time series of bias and RMSD for *QALL* at 500 hPa for the 3-h forecast period. Bias is small for all experiments, showing a transition from slightly too dry to slightly too wet with time, consistent with the QVAPOR results. Although the SAT experiment improved the *QALL* analysis at 1200 UTC, its impact becomes insignificant 1 h into the forecast (Fig. 7b), with CONV and SAT producing similar RMSD values ( $\sim 0.34 \text{ g kg}^{-1}$ ). The RAD experiment contains lower RMSD than CONV at all forecast times, but the improvement also decreases quickly as a function of time. The RADSAT experiment, however, remains the most accurate case at all times despite the detrimental impacts of the satellite data after the 1-h forecast, suggesting that the radar observations may be constraining errors introduced by the satellite observations. The high-resolution cloud characteristics added to the model analysis by assimilating these data are apparently lost during the forecast period as the ensemble members begin to diverge, washing out the high-resolution detail in the ensemble mean. This is consistent with the results shown in Otkin (2012b) for the same case study. Similar error characteristics were observed at 850 hPa, but with SAT only producing a small decrease in RMSD even at 1200 UTC (Fig. 8b). After 1300 UTC, SAT becomes

slightly worse than CONV while the improvement from assimilating radar data also disappears by the end of the 3-h forecast period. These results indicate that both datasets have less impact on the lower-level, liquid phase clouds.

Vertical profiles of bias and RMSD for *QALL* at 1300 and 1500 UTC are shown in Figs. 9a and 10a. For all experiments the bias is generally small at all levels. At 1300 UTC, SAT has slightly smaller RMSD than CONV between 650 and 500 hPa with limited improvements elsewhere. Much smaller errors occurred during RAD with improvements spread over a larger vertical depth. By 1500 UTC, no improvements are evident in the SAT case, with larger RMSD occurring at some levels (Fig. 10a). Some improvements are maintained during the RAD experiment, though again the magnitude has decreased substantially. In summary, the results indicate that assimilating  $6.95\text{-}\mu\text{m } T_B$  does not provide a long lasting forecast impact during this case study, whereas assimilating radar data provided some additional skill compared to CONV, but by 1500 UTC its impact is also weak.

### c. Hydrometeor species

Next, we examine the forecast impact on the cloud hydrometeor species. Figure 8d shows time series of 850-hPa *QCLOUD* bias and RMSD for each experiment

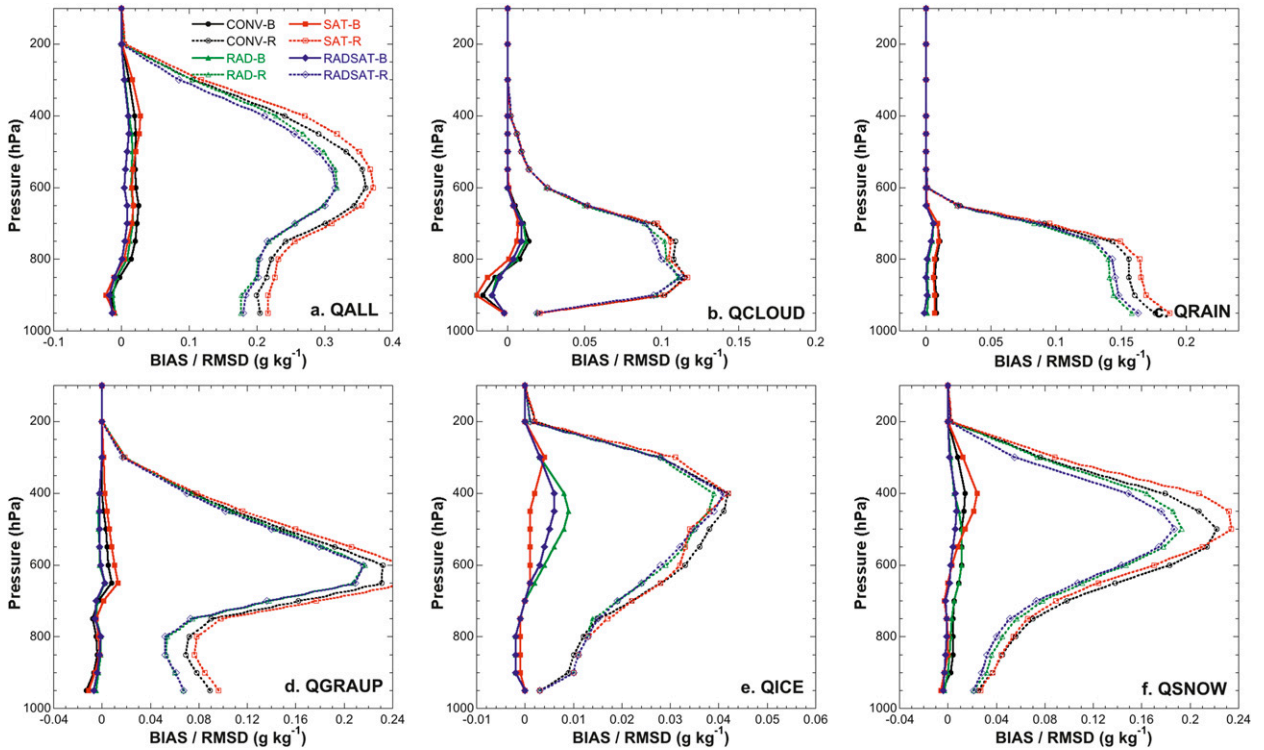


FIG. 10. As in Fig. 6, but for 3-h forecasts at 1500 UTC.

during the forecast period. At 1300 UTC, CONV and SAT have similar errors with RAD and RADSAT containing slightly lower RMSD; however, by 1500 UTC, all experiments have similar errors. The importance of assimilating radar data is much more apparent in QRAIN because radar reflectivity is directly sensitive to liquid water drops. RAD lowers RMSD compared to CONV by  $0.06 \text{ g kg}^{-1}$  at 1200 UTC with the improvement decreasing with time (Fig. 8e). Despite the more limited impact of satellite data on QRAIN evidenced by the similar CONV and SAT errors, the overall RADSAT experiment generally has the lowest errors. The vertical profiles of QRAIN bias and RMSD show that the impact of radar reflectivity is consistent throughout the layer where liquid drops are present (below 600 hPa) (Figs. 9c and 10c).

QGRAUP represents an interesting hydrometeor species in the form of elevated frozen drop-sized particles. At 1200 UTC, Jones et al. (2013a) found that both SAT and RAD lowered QGRAUP RMSD compared to CONV. However, the QGRAUP time series of bias and RMSD for both 850 and 500 hPa shows that the impact of satellite and radar data decreases rapidly resulting in limited improvement by 1300 UTC. At 500 hPa, RAD and RADSAT are more accurate than CONV after 1400 UTC while RADSAT maintains the lowest RMSD at all forecast times despite the corresponding SAT and RAD experiments losing any improvement (Fig. 7c).

This indicates the potential value of assimilating both observation types.

Finally, we examine QICE and QSNOW variables as a function of forecast time. For QICE at 500 hPa, RMSD values are very low corresponding to low overall QICE concentrations in the domain. RAD and RADSAT both contain slightly lower RMSD at all forecast times. Much larger differences are apparent in QSNOW at 500 hPa (Fig. 7e). Both SAT and especially RAD reduce RMSD with the former maintaining skill out to 1330 UTC and the latter until the end of the forecast period at 1500 UTC. As with QRAIN and QGRAUP, QSNOW represents a hydrometeor directly observable by radar reflectivity, though with somewhat less sensitivity. The greatest improvement from either satellite or radar data occurs between 600 and 400 hPa (Fig. 9f), consistent with the 1200 UTC findings summarized above and in Jones et al. (2013a). The pattern remains consistent out to 1500 UTC except that the SAT and CONV RMSD profiles become similar (Fig. 10f).

## 7. Simulated radar and satellite data forecasts

### a. GOES-R ABI $6.95\text{-}\mu\text{m } T_B$

To assess the impact of assimilating remote sensing data on more complex products, we compare the ensemble

mean satellite  $T_B$  and radar reflectivity from each experiment with the corresponding truth simulation as a function of forecast time. In addition to calculating bias and RMSD statistics for each experiment, skill scores including the probability of detection (POD), false alarm rate (FAR), and Heidke skill score (HSS) are also computed using a threshold of  $6.95\text{-}\mu\text{m } T_B < 230\text{ K}$  (Wilkes 2006). If both the truth and experiment forecast have a pixel where  $6.95\text{-}\mu\text{m } T_B < 230\text{ K}$  then this is considered a “hit.” If the experiment contains a pixel with  $6.95\text{-}\mu\text{m } T_B < 230\text{ K}$  and this threshold is not exceeded in truth, then it is considered a false detection. Finally, if neither truth nor the experiment exceeds this threshold, then it is considered a correct null forecast. The goal is to generate a forecast where “hits” are maximized, resulting in a high POD, but false detections are limited, thereby resulting in a low FAR. The HSS takes both into account to generate a statistic indicating the overall skill of the experiment at forecasting  $T_B$ .

Jones et al. (2013a) found that the final  $6.95\text{-}\mu\text{m } T_B$  analyses from the SAT, RAD, and RADSAT cases are characterized by higher POD and HSS scores and lower FAR than CONV with SAT having the highest skill (Fig. 11). The rapid decrease in skill among the hydrometeor variables noted in the previous section suggests that the improvements to simulated  $6.95\text{-}\mu\text{m } T_B$  should also decrease with time. The skill score statistics by 1300 UTC strongly indicate that this is indeed the case. Skill scores for all four experiments converge by 1300 UTC indicating that any skill from assimilating either satellite or radar data is mostly lost early in the forecast period. For example, HSS falls from 0.71 at 1200 UTC to below 0.4 by 1300 UTC for the SAT experiment (Fig. 11c). Thereafter, HSS for all experiments remain near 0.4. Inspection of the simulated satellite output at 1300 UTC (Fig. 12) shows that assimilating satellite or radar data appears to capture some of the detailed structures in the cloud fields better than CONV. All experiments exhibit a cold  $T_B$  bias relative to truth that is mostly eliminated at 1200 UTC (Jones et al. 2013a), indicating that the experiments may contain excessive cloud cover. This is most apparent along the convection in eastern Arkansas and Louisiana and also in the more stratiform clouds across Missouri and Oklahoma. Thus, it appears that  $6.95\text{-}\mu\text{m } T_B$  and radar reflectivity data have a limited impact on simulated satellite imagery during the forecast period, at least as computed using traditional grid-point verification statistics.

### b. WSR-88D reflectivity

A similar comparison is conducted using simulated radar reflectivity data at 2 and 6 km to determine the relative impacts of the observations on the radar reflectivity

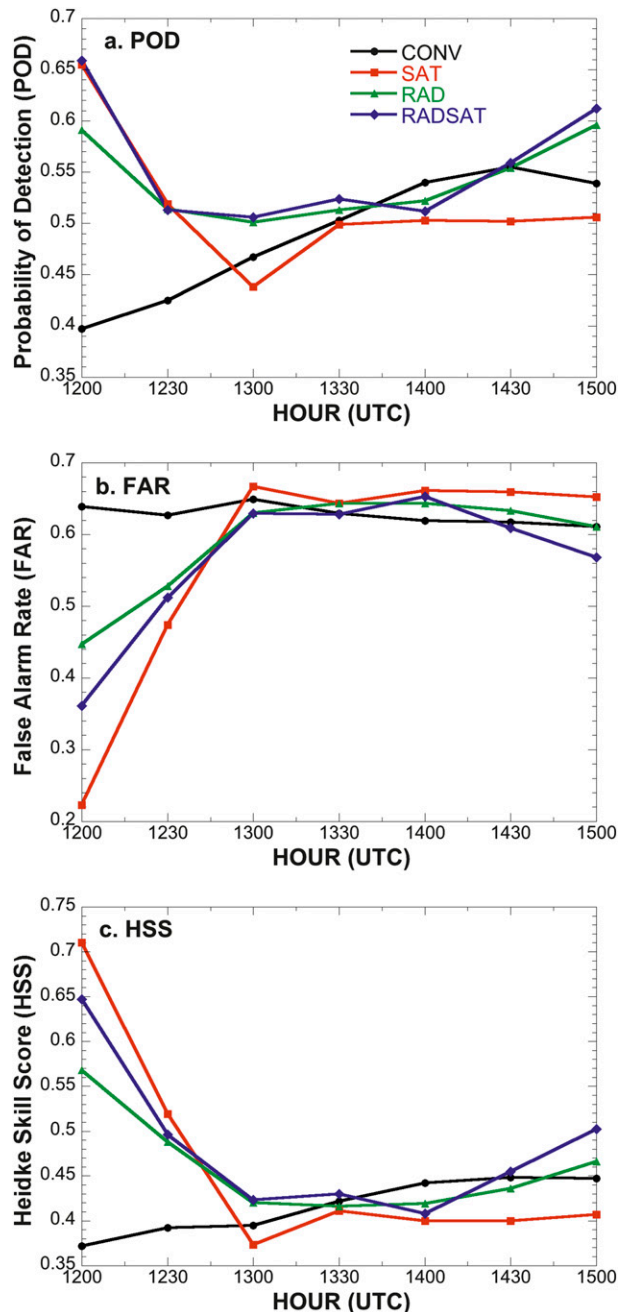


FIG. 11. Time series of (a) POD, (b) FAR, and (c) HSS between 1200 and 1500 UTC for simulated ABI  $6.95\text{-}\mu\text{m } T_B$  forecast from each experiment.

analysis. Skill scores are computed in the same manner as employed for the satellite data, but now using a threshold of  $>25\text{ dBZ}$ . Results show that assimilating radar data provides a longer lasting impact to simulated reflectivity forecasts at 2 and 6 km AGL compared to its impact on simulated satellite data (Fig. 13), as would be expected. At 2 km, RAD and RADSAT generate a

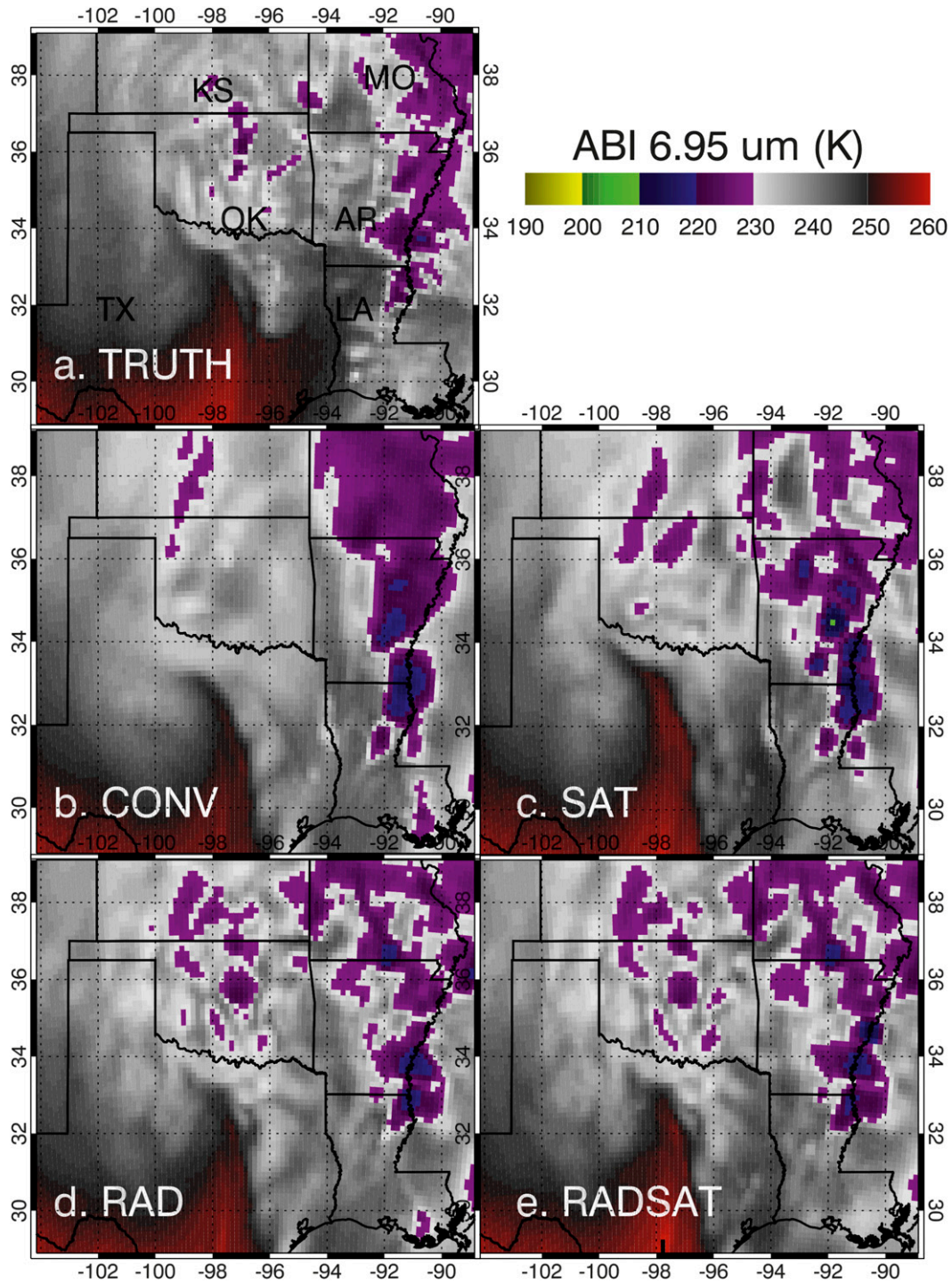


FIG. 12. Simulated GOES-R ABI 6.95- $\mu\text{m}$   $T_B$  (K) for the truth simulation and each experiment at 1300 UTC 24 Dec.

POD significantly greater than CONV until 1500 UTC (Fig. 13a). Even SAT performs slightly better despite this being a lower-tropospheric level. Similar results are present for FAR and HSS with RAD and RADSAT being the best performers. However, SAT is also noticeably

better than CONV at most forecast times. At this level, SAT maintains some skill longer compared to the corresponding forecasts of simulated 6.95- $\mu\text{m}$   $T_B$ .

Comparing the 2-km simulated radar reflectivity forecasts at 1300 UTC with truth data shows that all

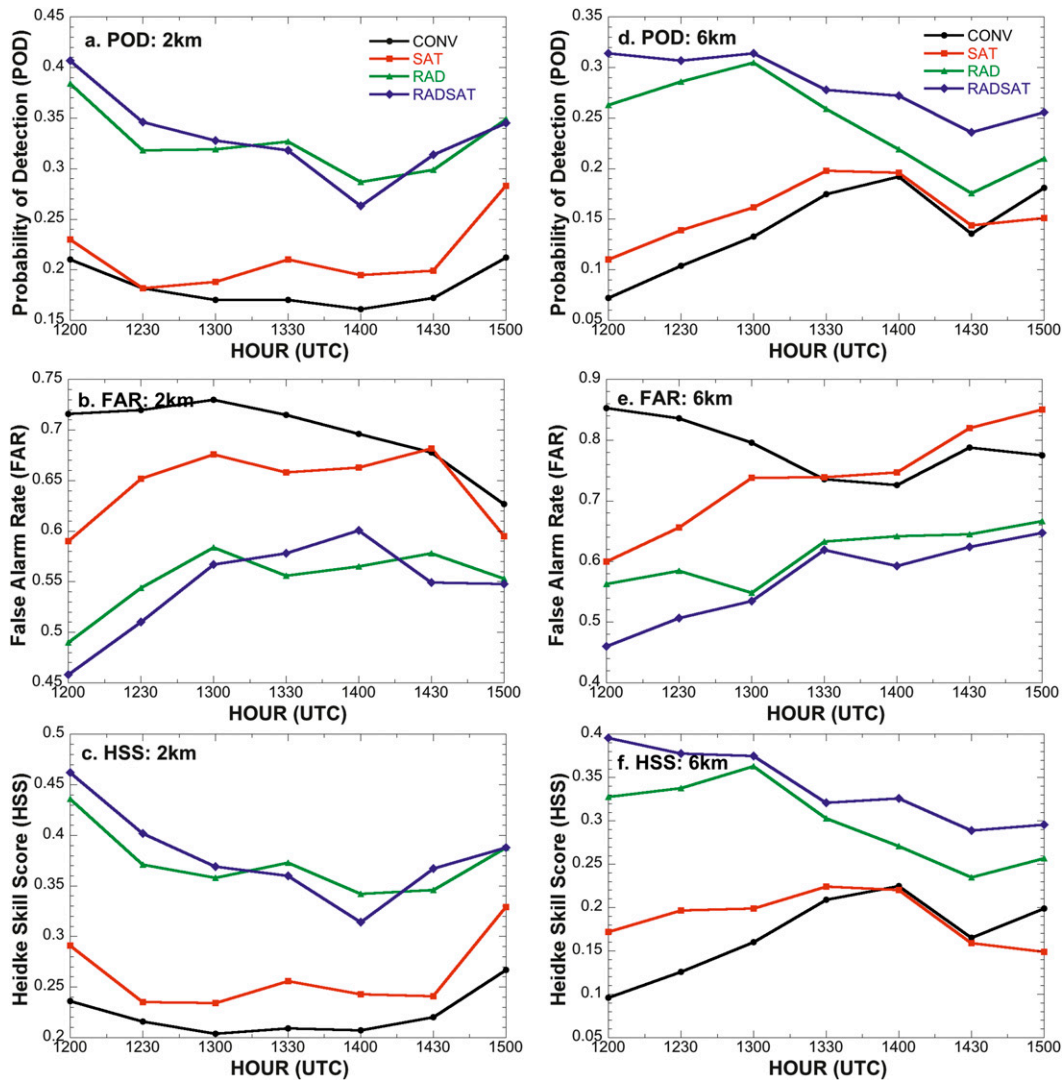


FIG. 13. Time series of (a) POD, (b) FAR, and (c) HSS between 1200 and 1500 UTC for 2-km AGL simulated WSR-88D reflectivity forecasts. (d)–(f) As in (a)–(c), but for 6-km AGL reflectivity forecasts.

experiments contain excessively large areas of higher reflectivity (Fig. 14). Several areas of high-reflectivity values correspond with the locations of low  $6.95\text{-}\mu\text{m } T_B$  in Fig. 12. The primary difference between SAT and RAD is that the latter better captures the higher-resolution reflectivity characteristics present in the truth analysis, which is reflected in the better skill scores (Fig. 13). Similar results were found at 6 km AGL (not shown) with RAD maintaining higher skill than CONV until 1500 UTC with the improvement generally decreasing with time. Initially, SAT generates a comparable FAR to the RAD experiment, but the improvement relative to CONV diminishes by 1330 UTC. The improvements in POD and HSS become small by 1330 UTC, which is a similar time frame as observed

in the simulated satellite and cloud hydrometeor forecasts.

## 8. Conclusions

Detailed analysis of the relationship between water vapor and cloud hydrometeor variables and  $6.95\text{-}\mu\text{m } T_B$  and radar reflectivity show that assimilating both data types improves the analysis accuracy. For most cases, the magnitude of the correlation coefficients and their altitude correspond well with where the greatest reduction in RMSD occurs between CONV and either SAT or RAD. These results further support the findings by Jones et al. (2013a) who concluded that assimilating these data did indeed generate improved model analyses.

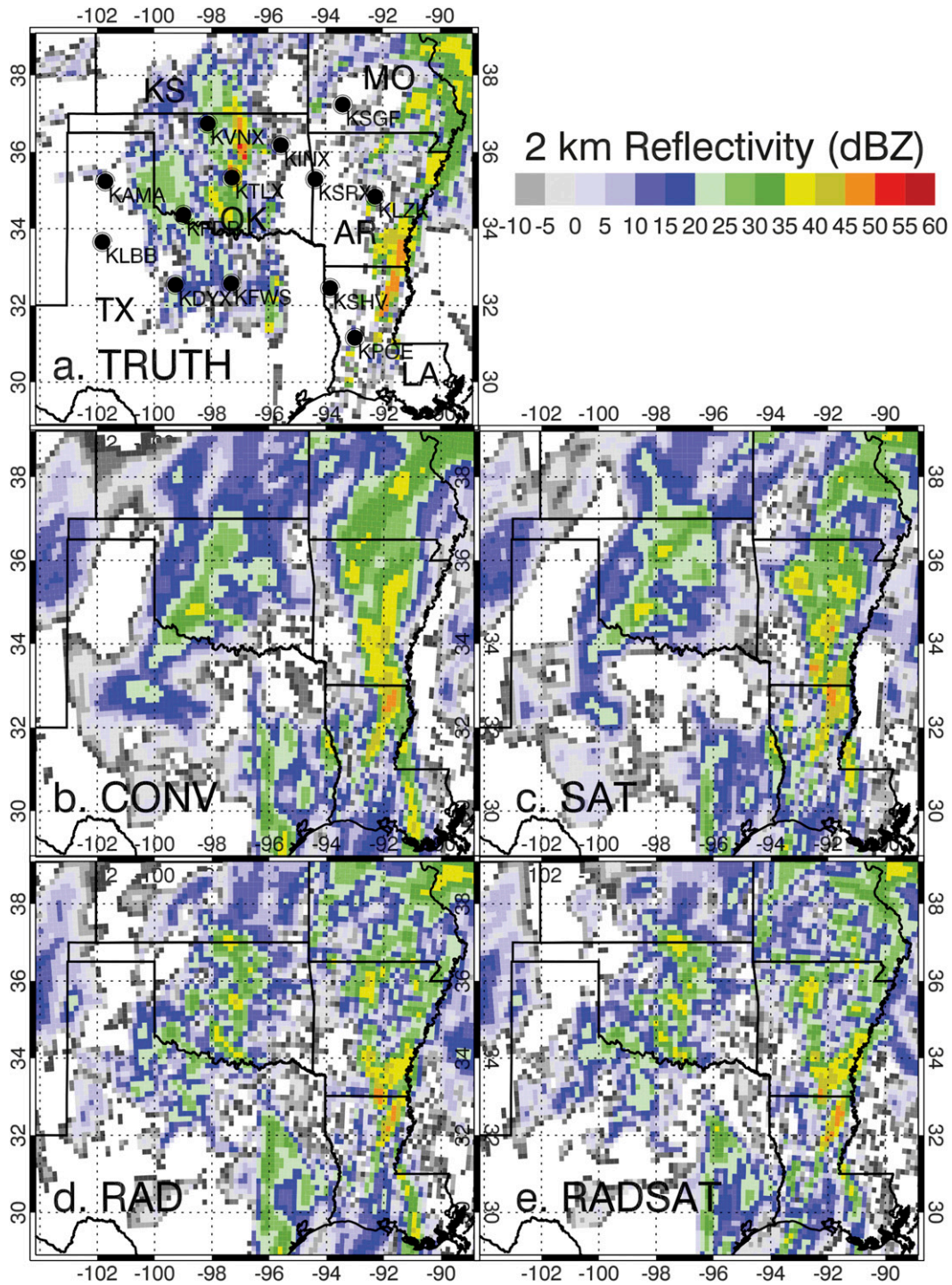


FIG. 14. Simulated WSR-88D 2-km AGL radar reflectivity at 1300 UTC for the truth simulation and each experiment.

The improved analysis accuracy leads to better water vapor and cloud hydrometeor forecasts, though the forecast impact of satellite data and radar reflectivity varies greatly with variable and forecast time. Assimilating  $6.95\text{-}\mu\text{m } T_B$  had the greatest positive impact on

midtropospheric water vapor content that remains evident 3 h into the forecast. However, water vapor forecasts nearer the surface from SAT actually performed worse than CONV alone. This indicates the need for additional satellite derived moisture information at these

levels. The GOES-R ABI will provide this information in the form of a 7.34- $\mu\text{m}$  channel, which initial testing shows an improved lower-tropospheric moisture analysis compared to assimilating the 6.95- $\mu\text{m}$  channel. The effects of satellite data on cloud hydrometeor variables are also pronounced, but the positive impacts generally only last approximately 1 h during the forecast. Generally, SAT performs better with the analysis and forecast of frozen hydrometeor variables such as QICE and QSNOW in the mid- and upper troposphere compared to lower-level liquid hydrometeors. One concern is that the assimilation of satellite data degrades the low level forecasts of certain variables (QRAIN, QVAPOR) near 850 hPa as forecast time increases beyond 1 h.

Assimilating simulated radar observations generally improves analysis and forecast fields of water vapor and cloud hydrometeor variables more than the satellite data. The improvement is apparent at most atmospheric levels and not confined to the mid- and upper troposphere. This is due in large part to the much greater number of radar observations being assimilated and their high vertical resolution compared to the single atmospheric column nature of individual satellite observations. Assimilating radar data is most effective at improving skill in the larger hydrometeor variables such as QRAIN, QGRAUP, and QSNOW, where sensitivity to radar reflectivity is the greatest. Both lower- and midtropospheric radar observations have positive impacts on the forecasts, generally maximized in the layers surrounding the observation. The larger overall positive impact from radar data assimilation generally results in better downstream forecasts compared to SAT. The 6.95- $\mu\text{m}$   $T_B$  provide the most lasting positive impact on 500-hPa QVAPOR while radar reflectivity also improves QVAPOR and QRAIN consistently out to 3 h. Otherwise, even the positive impacts from radar data are small 3 h into the forecast.

Several challenges and avenues for future research exist building on the results and lessons learned as a part of this research. One need is to determine the impact of different error characteristics of clear and cloudy satellite observations, as they are likely different from the constant assumption used here for all observations. Also, the impacts of multichannel satellite data assimilation combined with radar observations should be assessed. It is likely that including more satellite channels sensitive to different layers of the atmosphere will provide additional vertical profile information, increasing its relevance relative to radar observations. Development of vertical localization techniques for satellite radiances should also improve the satellite data impact by constraining their influence only to layers where they are most sensitive. These and other topics will be explored

by the authors in future studies using simulated and real-data experiments.

*Acknowledgments.* This work was funded by the National Oceanic and Atmospheric Administration (NOAA) under Grant NA10NES4400013 as well as NOAA/Office of Oceanic and Atmospheric Research under the NOAA–University of Oklahoma Cooperative Agreement NA11OAR4320072, U.S. Department of Commerce. Additional support was provided by the NOAA/National Environmental Satellite, Data, and Information Service (NESDIS). The assimilation experiments were performed using the NOAA/NESDIS/STAR “S4” supercomputer located at the University of Wisconsin–Madison and the “ranger” supercomputer located at the Texas Advanced Computing Center. Ranger is part of the Extreme Science and Engineering Discovery Environment (XSEDE) network that is supported by the National Science Foundation under Grant OCI-1053575.

#### REFERENCES

- Aksoy, A., D. Dowell, and C. Snyder, 2009: A multicase comparative assessment of the ensemble Kalman filter for assimilation of radar observations. Part I: Storm-scale analyses. *Mon. Wea. Rev.*, **137**, 1805–1824.
- , —, and —, 2010: A multicase comparative assessment of the ensemble Kalman filter for assimilation of radar observations. Part II: Short-range ensemble forecasts. *Mon. Wea. Rev.*, **138**, 1273–1292.
- Anderson, J. L., T. Hoar, K. Raeder, H. Liu, N. Collins, R. Torn, and A. Avellano, 2009: The Data Assimilation Research Testbed: A community data assimilation facility. *Bull. Amer. Meteor. Soc.*, **90**, 1283–1296.
- Andersson, E., A. Hollingsworth, G. Kelly, P. Lönnberg, J. Pailleux, and Z. Zhang, 1991: Global observing system experiments on operational statistical retrievals of satellite sounding data. *Mon. Wea. Rev.*, **119**, 1851–1864.
- Bouttier, F., and G. Kelly, 2001: Observing-system experiments in the ECMWF 4D-Var data assimilation system. *Quart. J. Roy. Meteor. Soc.*, **127**, 1469–1488.
- Chevallier, F., P. Lopez, A. M. Tompkins, M. Janiskova, and E. Moreau, 2004: The capability of 4D-Var systems to assimilate cloud-affected satellite infrared radiances. *Quart. J. Roy. Meteor. Soc.*, **130**, 917–932.
- Collard, A. D., and A. P. McNally, 2009: The assimilation of Infrared Atmospheric Sounding Interferometer radiances at ECMWF. *Quart. J. Roy. Meteor. Soc.*, **135**, 1044–1058.
- Crum, T. D., and R. L. Alberty, 1993: The WSR-88D and the WSR-88D Operational Support Facility. *Bull. Amer. Meteor. Soc.*, **74**, 1669–1687.
- Derber, J. C., and W. S. Wu, 1998: The use of TOVS cloud-cleared radiances in the NCEP SSI analysis system. *Mon. Wea. Rev.*, **126**, 2287–2299.
- Dowell, D. C., G. S. Romine, and C. Snder, 2010: Ensemble storm-scale data assimilation and prediction for severe convective storms. Preprints, *25th Conf. on Severe Local Storms*, Denver, CO, Amer. Meteor. Soc., 9.5. [Available online at <https://ams.confex.com/ams/pdfpapers/176121.pdf>.]

- , L. J. Wicker, and C. Snyder, 2011: Ensemble Kalman filter assimilation of radar observations of the 8 May 2003 Oklahoma City supercell: Influences of reflectivity observations on storm-scale analyses. *Mon. Wea. Rev.*, **139**, 272–294.
- English, S. J., and U. Une, 2006: Assimilation of AMSU cloudy radiances. Preprints, *15th Int. TOVS Study Conf.*, Maratea, Italy, International TOVS Working Group, 447–454.
- Evensen, G., 1994: Sequential data assimilation with a nonlinear quasi-geostrophic model using Monte Carlo methods to forecast error statistics. *J. Geophys. Res.*, **99** (C5), 10 143–10 162.
- Gao, J., and D. J. Stensrud, 2012: Assimilation of reflectivity data in a convective-scale, cycled 3DVAR framework with hydro-meteor classification. *J. Atmos. Sci.*, **69**, 1054–1065.
- , M. Xue, A. Shapiro, and K. K. Droegemeier, 1999: A variational method for the retrieval of three-dimensional wind fields from dual-Doppler radars. *Mon. Wea. Rev.*, **127**, 2128–2142.
- , —, K. Brewster, and K. K. Droegemeier, 2004: A three-dimensional variational data assimilation method with a recursive filter for single-Doppler radar. *J. Atmos. Oceanic Technol.*, **21**, 457–469.
- Heemink, A. W., M. Verlaan, and A. J. Segers, 2001: Variance reduced ensemble Kalman filtering. *Mon. Wea. Rev.*, **129**, 1718–1728.
- Heidinger, A. K., C. O'Dell, R. Bennartz, and T. Greenwald, 2006: The successive-order-of-interaction radiative transfer model. Part I: Model development. *J. Appl. Meteor. Climatol.*, **45**, 1388–1402.
- Hong, S.-Y., and J.-O. Lim, 2006: The WRF single-moment 6-class microphysics scheme (WSM6). *J. Korean Meteor. Soc.*, **42**, 129–151.
- , Y. Noh, and J. Dudhia, 2006: A new vertical diffusion package with an explicit treatment of entrainment processes. *Mon. Wea. Rev.*, **134**, 2318–2341.
- Iacono, M. J., J. S. Delamere, E. J. Mlawer, M. W. Shephard, S. A. Clough, and W. D. Collins, 2008: Radiative forcing by long-lived greenhouse gases: Calculations with the AER radiative transfer models. *J. Geophys. Res.*, **113**, D13103, doi:10.1029/2008JD009944.
- Jones, T. A., J. Otkin, D. J. Stensrud, and K. Knopfmeier, 2013a: Assimilation of satellite infrared radiances and Doppler radar observations during a cool season Observing System Simulation Experiment. *Mon. Wea. Rev.*, **141**, 3273–3299.
- , D. J. Stensrud, P. Minnis, and R. Palikonda, 2013b: Evaluation of a forward operator to assimilate cloud water path into WRF-DART. *Mon. Wea. Rev.*, **141**, 2272–2289.
- Kain, J. S., 2004: The Kain–Fritsch convective parameterization: An update. *J. Appl. Meteor.*, **43**, 170–181.
- , and J. M. Fritsch, 1993: Convective parameterization for mesoscale models: The Kain–Fritsch scheme. *The Representation of Cumulus Convection in Numerical Models*, Meteor. Monogr., No. 24, Amer. Meteor. Soc., 165–170.
- Kalman, R. E., 1960: A new approach to linear filtering and prediction problems. *J. Basic Eng.*, **82**, 35–45.
- Le Marshall, J., and Coauthors, 2006: Improving global analysis and forecasting with AIRS. *Bull. Amer. Meteor. Soc.*, **87**, 891–894.
- Li, J., and H. Liu, 2009: Improved hurricane track and intensity forecast using single field-of-view advanced IR sounding measurements. *Geophys. Res. Lett.*, **36**, L11813, doi:10.1029/2009GL038285.
- Liu, H., and J. Li, 2010: An improvement in forecasting rapid intensification of Typhoon Sinlaku (2008) using clear sky full spatial resolution advanced IR soundings. *J. Appl. Meteor. Climatol.*, **49**, 821–827.
- McCarty, W., G. Jedloveck, and T. L. Miller, 2009: Impact of the assimilation of Atmospheric Infrared Sounder radiance measurements on short-term weather forecasts. *J. Geophys. Res.*, **114**, D18122, doi:10.1029/2008JD011626.
- McNally, A. P., 2009: The direct assimilation of cloud-affected satellite infrared radiances in the ECMWF 4D-Var. *Quart. J. Roy. Meteor. Soc.*, **135**, 1214–1229.
- , J. C. Derber, W. Wu, and B. B. Katz, 2000: The use of TOVS level-1b radiances in the NCEP SSI analysis system. *Quart. J. Roy. Meteor. Soc.*, **126**, 689–724.
- , P. D. Watts, J. A. Smith, R. Engelen, G. A. Kelly, J. N. Thepaut, and M. Matricardi, 2006: The assimilation of AIRS radiance data at ECMWF. *Quart. J. Roy. Meteor. Soc.*, **132**, 935–957.
- Mo, K. C., X. L. Wang, R. Kistler, M. Kanamitsu, and E. Kalnay, 1995: Impact of satellite data on the CDAS-reanalysis system. *Mon. Wea. Rev.*, **123**, 124–139.
- Moreau, E., P. Lopez, P. Bauer, A. M. Tompkins, M. Janisková, and F. Chevallier, 2004: Variational retrieval of temperature and humidity profiles using rain rates versus microwave brightness temperatures. *Quart. J. Roy. Meteor. Soc.*, **130**, 827–852.
- Otkin, J. A., 2010: Clear and cloudy sky infrared brightness temperature assimilation using an ensemble Kalman filter. *J. Geophys. Res.*, **115**, D19207, doi:10.1029/2009JD013759.
- , 2012a: Assessing the impact of the covariance localization radius when assimilating infrared brightness temperature observations using an ensemble Kalman filter. *Mon. Wea. Rev.*, **140**, 543–561.
- , 2012b: Assimilation of water vapor sensitive infrared brightness temperature observations during a high impact weather event. *J. Geophys. Res.*, **117**, D19203, doi:10.1029/2012JD017568.
- , D. C. Hartung, D. D. Turner, R. A. Petersen, W. F. Feltz, and E. Janson, 2011: Assimilation of surface-based boundary layer profiler observations during a cool-season weather event using an observing system simulation experiment. Part I: Analysis impact. *Mon. Wea. Rev.*, **139**, 2309–2326.
- Polkinghorne, R., and T. Vukicevic, 2011: Data assimilation of cloud affected radiances in a cloud resolving model. *Mon. Wea. Rev.*, **139**, 755–773.
- Reale, O., J. Susskind, R. Rosenberg, E. Brin, E. Liu, L. P. Riishojgaard, J. Terry, and J. C. Jusem, 2008: Improving forecast skill by assimilation of quality-controlled AIRS temperature retrievals under partially cloudy conditions. *Geophys. Res. Lett.*, **35**, L08809, doi:10.1029/2007GL033002.
- Rodgers, C. D., 2000: *Inverse Methods for Atmospheric Sounding: Theory and Practice*. World Scientific Publishing Company, 200 pp.
- Schmit, T. J., M. M. Gunshor, W. P. Menzel, J. J. Gurka, J. Li, and A. S. Bachmeier, 2005: Introducing the next-generation Advanced Baseline Imager on GOES-R. *Bull. Amer. Meteor. Soc.*, **86**, 1079–1096.
- Seaman, C. J., M. Sengupta, and T. H. Vonder Haar, 2010: Mesoscale satellite data assimilation: Impact of cloud-affected infrared observations on a cloud-free initial model state. *Tellus*, **62A**, 298–318.
- Skamarock, W. C., and Coauthors, 2008: A description of the Advanced Research WRF version 3. NCAR Tech. Note

- NCAR/TN-475+STR, 113 pp. [Available from UCAR Communications, P.O. Box 3000, Boulder, CO 80307.]
- Snyder, C., and F. Zhang, 2003: Assimilation of simulated Doppler radar observations with an ensemble Kalman filter. *Mon. Wea. Rev.*, **131**, 1663–1677.
- Stengel, M., M. Lindskog, P. Unden, N. Gustafsson, and R. Bennartz, 2010: An extended observation operator in HIRLAM 4D-VAR for the assimilation of cloud-affected satellite radiances. *Quart. J. Roy. Meteor. Soc.*, **136**, 1064–1074.
- Stensrud, D. J., and Coauthors, 2009: Convective-Scale Warn-on-Forecast System. *Bull. Amer. Meteor. Soc.*, **90**, 1487–1499.
- Vukicevic, T., T. Greenwald, M. Zupanski, D. Zupanski, T. Vonder Haar, and A. Jones, 2004: Mesoscale cloud state estimation from visible and infrared satellite radiances. *Mon. Wea. Rev.*, **132**, 3066–3077.
- , M. Sengupta, A. S. Jones, and T. Vonder Haar, 2006: Cloud-resolving satellite data assimilation: Information content of IR window observations and uncertainties in estimation. *J. Atmos. Sci.*, **63**, 901–919.
- Weng, F., T. Zhu, and B. Yan, 2007: Satellite data assimilation in numerical weather prediction models. Part II: Uses of rain-affected radiances from microwave observations for hurricane vortex analysis. *J. Atmos. Sci.*, **64**, 3910–3925.
- Weygandt, S. S., A. Shapiro, and K. K. Droegemeir, 2002: Retrieval of model initial fields from single-Doppler observations of a supercell thunderstorm. Part I: Single-Doppler velocity retrieval. *Mon. Wea. Rev.*, **130**, 433–453.
- Wilks, D. S., 2006: *Statistical Methods in the Atmospheric Sciences*. 2nd ed. Academic Press, 627 pp.
- Xiao, Q., Y.-H. Kuo, J. Sun, W.-C. Lee, E. Lim, Y.-R. Guo, and D. M. Barker, 2005: Assimilation of Doppler radar observations with a regional 3DVAR System: Impact of Doppler velocities on forecasts of a heavy rainfall case. *J. Appl. Meteor.*, **44**, 768–788.
- Xu, Q., H. Lu, S. Gao, M. Xue, and M. Tong, 2008: Time-expanded sampling for ensemble Kalman filter: Assimilation experiments with simulated radar observations. *Mon. Wea. Rev.*, **136**, 2651–2667.
- Yussouf, N., and D. J. Stensrud, 2010: Impact of phased-array radar observations over a short assimilation period: Observing system simulation experiments using an ensemble Kalman filter. *Mon. Wea. Rev.*, **138**, 517–538.
- Zhang, F., C. Snyder, and J. Sun, 2004: Impacts of initial estimate and observation availability on convective-scale data assimilation with an ensemble Kalman filter. *Mon. Wea. Rev.*, **132**, 1238–1253.